

RESEARCH ARTICLE

 View Article Online
View Journal | View Issue

 Cite this: *Inorg. Chem. Front.*, 2023, **10**, 638

Cationic pair substitution in $\text{LaAlO}_3:\text{Mn}^{4+}$ for octahedral-tilting-dependent zero-phonon line†

 Siyuan Li, ^a Chenyu Zhang,^a Qi Zhu ^{*a} and Ji-Guang Li ^{*b}

Zero-phonon line (ZPL) emission of Mn^{4+} , without the participation of phonons, is tightly related to the host crystal structure. However, the intensity of the intrinsic ZPL is much weaker than that of Stokes and anti-Stokes vibrational bands, and it always leads to a discontinuous emission peak. Regulating the ZPL of Mn^{4+} for a strong emission is very important but remains a challenge for perovskite-type oxides. Here, novel $\text{La}_{1-x}\text{Ba}_x\text{Al}_{1-x}\text{Ti}_x\text{O}_3:0.001\text{Mn}^{4+}$ (LBAT:0.001 Mn^{4+} , $x = 0-0.2$) and $\text{La}_{1-y}\text{Y}_y\text{Al}_{1-y}\text{Ga}_y\text{O}_3:0.001\text{Mn}^{4+}$ (LYAG:0.001 Mn^{4+} , $y = 0-0.2$) samples were successfully synthesized through a high-temperature solid-state reaction, and a tunable ZPL of Mn^{4+} was found by cationic pair substitution of $\text{Ba}^{2+}-\text{Ti}^{4+}$ and $\text{Y}^{3+}-\text{Ga}^{3+}$ for $\text{La}^{3+}-\text{Al}^{3+}$ in $\text{LaAlO}_3:\text{Mn}^{4+}$. The ZPL intensity is related to the local symmetry around Mn^{4+} and the ZPL energy corresponds to the Mn–O bond distance and the O–Mn–O bond distortion. Through co-doping $\text{Ba}^{2+}-\text{Ti}^{4+}$, the ZPL at 710 nm is enhanced and the intensity increases continuously with increasing the x value, due to the local symmetric degree of Mn^{4+} decreasing slowly. However, $\text{Y}^{3+}-\text{Ga}^{3+}$ co-doping induces a linear and quick increase in the intensity of ZPL at 704 nm with increasing y value, due to the local symmetric degree of Mn^{4+} decreasing quickly. The octahedral tilting distortion is very important for the local symmetry. $\text{Ba}^{2+}-\text{Ti}^{4+}$ co-doping reduces octahedral tilting distortion, but $\text{Y}^{3+}-\text{Ga}^{3+}$ co-doping induces a serious octahedral tilting distortion. Consequently, the ZPL emission exhibits an octahedral-tilting dependent behavior. Mainly due to the larger distortion of the O–Mn–O bond, the energy of ZPL for LYAG:0.001 Mn^{4+} is higher than that for LBAT:0.001 Mn^{4+} . The outcomes of this work provide a promising way to regulate the ZPL intensity and energy by tuning the local structure around Mn^{4+} , and may have wide implications for Mn^{4+} -doped phosphors and solid-state lighting.

 Received 3rd August 2022,
Accepted 26th November 2022
DOI: 10.1039/d2qi01683d
rsc.li/frontiers-inorganic

1. Introduction

The ABO_3 perovskite oxides present a multitude of functional properties and are widely renowned for their potential in various types of applications, owing to their low cost and high abundance.^{1,2} For the simple ABO_3 perovskite, the A cation connects to 12 oxygen atoms to form an AO_{12} dodecahedron, and the B cation links with 6 oxygen atoms to form a BO_6 octahedron. The BO_6 are connected to each other by O vertices to form a three-dimensional framework structure, and A cations are located in the cavities surrounded by eight BO_6 octahedra.^{3,4} The most common distortion for ABO_3 perovskite oxide is octahedral tilting, which is related to the rigid BO_6 ratios while keeping their

corner-sharing connectivity.^{5,6} Controlling the degree of octahedral tilting is of great interest, owing to its significant effects on the physical and chemical properties.

LaAlO_3 has rhombohedral symmetry with the pseudo-cubic cell parameters $a = b = c = 3.79 \text{ \AA}$ and $\beta = 90.066^\circ$, and it is one of the most important ABO_3 perovskite oxides.^{7,8} It is widely known that the phase transition from cubic to rhombohedral takes place at $T_c \approx 817 \text{ K}$ through AlO_6 octahedron rotation along $\langle -11-1 \rangle$ with half of the polyhedrons tilting clockwise and half tilting anticlockwise.⁹ During the rotation, the local structure changes a lot, which can be determined by the analysis of cell parameter variation and Raman spectra. Furthermore, structural changes from rhombohedral to cubic with increasing hydrostatic pressure are also observed, which are induced by decreasing AlO_6 octahedron tilting.¹⁰ Changes in the temperature and pressure not only alter the tilting degree of AlO_6 , but also lead to the replacement of La^{3+} or/and Al^{3+} by other cations.^{11,12} For example, when Nd^{3+} cations substitute for La^{3+} in LaAlO_3 , the AlO_6 octahedron tilting increases gradually.¹¹ The octahedron tilting distortions will induce huge variations in the local structure and produce an impact on the properties of the functional materials.⁷

^aKey Laboratory for Anisotropy and Texture of Materials (Ministry of Education), School of Materials Science and Engineering, Northeastern University, Shenyang, Liaoning 110819, China. E-mail: zhuq@smm.neu.edu.cn; Tel: +86-24-8367-2700

^bResearch Center for Functional Materials, National Institute for Materials Science, Namiki 1-1, Tsukuba, Ibaraki 305-0044, Japan. E-mail: LI.Jiguang@nims.go.jp; Tel: +81-29-860-4394

† Electronic supplementary information (ESI) available. See DOI: <https://doi.org/10.1039/d2qi01683d>

LaAlO₃ is an appropriate host for Mn⁴⁺ doping to generate near-infrared emission.¹² Mn⁴⁺ with 3d³ electronic configuration is an excellent luminescent center.^{13,14} Usually, Mn⁴⁺ prefers to occupy the octahedral sites to generate the luminescence, which depends on the covalence and local coordination symmetry around Mn⁴⁺ in the host. The emission peak of Mn⁴⁺ corresponding to ²E_g-⁴A_{2g} usually consists of the zero-phonon line (ZPL) transition and the vibrational sidebands of ZPL with phonon assistance (Stokes and anti-Stokes vibronic band) ranging from 600 to 800 nm.¹⁵ Compared with the phonon sidebands, the energy and intensity of ZPL are much more sensitive to the local coordinated environment. The reason is that no phonon participates in the ZPL emission process, which is only dependent on the host structure.^{16,17} Generally, the intensity of the ZPL is related to the structural symmetry around Mn⁴⁺. According to the Tanabe-Sugano diagram, the ZPL emission energy remains the same with changing the crystal field splitting. In fact, the energy of Mn⁴⁺ emission is based on Mn-ligand hybridization.^{18,19} Decreasing hybridization should lead to higher ²E_g energies and increase the emission energy. Furthermore, weaker hybridization can be induced *via* the increased Mn-ligand distance and/or distorted ligand-Mn-ligand bond angles.¹⁸ Mn⁴⁺-doped phosphors are usually used as the red component in LED devices. Interestingly, when the ZPL is located at a wavelength smaller than 700 nm, the color rendering index of LED devices can be further improved by enhancing the ZPL emission, which is very important to obtain high-quality white LED devices.¹⁴ Because the ZPL of the LaAlO₃:Mn⁴⁺ phosphor is located at a wavelength larger than 700 nm, enhancing the ZPL cannot improve the color rendering index of the white LED device. However, LaAlO₃:Mn⁴⁺ phosphors can be used as LED devices, which are beneficial for plant growing.¹³ At the same time, a higher ZPL intensity can induce the two divided emission peaks (Stokes and anti-Stokes) to become a broad band, and then make the emission spectra a better match with the P_{FR} region of the plant absorption spectrum. Consequently, the luminous efficiency of phosphor with a continuous and broad emission band is higher than that of phosphor with a divided emission band.¹² Therefore, exploring the changes in ZPL energy and intensity with the local structure is vital for designing high-efficiency deep-red or near-infrared phosphors.

In our previous work,¹² zero-phonon line (ZPL) emission of Mn⁴⁺ was generated by substituting Mg²⁺-Ge⁴⁺ for Al³⁺-Al³⁺ in LaAlO₃:Mn⁴⁺, which resulted in significant octahedral tilting distortion and a mismatched cation size distortion. The local structure of Mn⁴⁺ is influenced by MgO₆ and GeO₆, which link to MnO₆ through the O vertex. In this way, the symmetry degree of Mn⁴⁺ decreases gradually along with increasing Mg²⁺-Ge⁴⁺ content, which induces an improvement in ZPL emission. However, the energy of ZPL emission is not discussed in detail in previous work, due to its insufficient impact on the local structure around Mn⁴⁺. In order to further reveal the relationship between the local coordinated environment around Mn⁴⁺ and the ZPL behavior (energy and intensity), a cationic pair substitution way to tune the local structure

is proposed here through replacing La³⁺-Al³⁺ rather than Al³⁺-Al³⁺ with Ba²⁺-Ti⁴⁺ and Y³⁺-Ga³⁺ in LaAlO₃:0.001Mn⁴⁺. BaO₁₂ and YO₁₂ polyhedrons connect with MnO₆ by sharing the same plane and edge, and GaO₆ and TiO₆ octahedra link to MnO₆ through the O vertex. So they would show a more serious effect on the local structure of Mn⁴⁺, compared with only sharing the same O vertex by Mg²⁺-Ge⁴⁺ substitution for Al³⁺-Al³⁺. Thus, in this work, La_{1-x}Ba_xAl_{1-x}Ti_xO₃:0.001Mn⁴⁺ (LBAT:0.001Mn⁴⁺, x = 0-0.2) and La_{1-y}Y_yAl_{1-y}Ga_yO₃:0.001Mn⁴⁺ (LYAG:0.001Mn⁴⁺, y = 0-0.2) samples were successfully synthesized through the high-temperature solid-state reaction in an atmospheric environment. The variations of the local structure were detected using XRD Rietveld refinement, Raman spectra, SEM and TEM analysis. The luminescence properties were obtained *via* the diffuse reflectance spectra, PLE spectra, PL spectra, lifetime decay curves and temperature-dependent PL spectra. Through the above analysis, the relationship between the local structure of Mn⁴⁺ and the ZPL behavior (energy and intensity) is discussed in detail.

2. Experimental section

2.1. Sample preparation

A series of La_{1-x}Ba_xAl_{1-x}Ti_xO₃:0.001Mn⁴⁺ (LBAT:0.001Mn⁴⁺, x = 0-0.25) and La_{1-y}Y_yAl_{1-y}Ga_yO₃:0.001Mn⁴⁺ (LYAG:0.001Mn⁴⁺, y = 0-0.25) samples were synthesized using the traditional high-temperature solid-phase reaction technique. La₂O₃, Al₂O₃, MnCO₃, BaCO₃, Y₂O₃, TiO₂ and Ga₂O₃ were used as the raw materials. La₂O₃ (99.99%) and Y₂O₃ (99.999%) were purchased from Huizhou Ruier Rare-Chem. Hi-Tech. Co. Ltd (Huizhou, China). Al₂O₃ (99.99%), MnCO₃ (99.95%), BaCO₃ (99.99%), TiO₂ (99.8%), and Ga₂O₃ (99.99%) were purchased from Aladdin Chemical Reagent Co. Ltd (Shanghai, China). La₂O₃ was heated at 1000 °C for 2 h before use for removing adsorbed water. The raw materials were accurately weighed according to the stoichiometric molar ratio of the designed compositions. Then, these raw materials were placed in an agate mortar and ground for 30 min to mix thoroughly. After that, the mixtures were preheated at 1000 °C for 5 h and then sintered at 1500 °C for 8 h in air. The final powders were obtained for further measurement after cooling down to room temperature naturally.

2.2. Characterization methods

The phase compositions of the samples were obtained by X-ray powder diffraction (XRD, model SmartLab, Rigaku, Tokyo, Japan) with the use of nickel-filtered Cu K α radiation (λ = 0.15406 nm) and 40 kV, 200 mA operating conditions. The scanning range was 10-90° and the scanning rate was 6° per minute. The XRD patterns for Rietveld refinement were acquired in the range of 10-110° at a step size of 0.02° with a step-scan mode of 2.5 s per step. The product morphology, microstructure and element mapping were analyzed through field emission scanning electron microscopy (FE-SEM, model JSM-7001F, JEOL, Tokyo) and transmission electron

microscopy (TEM, model JEM-2000FX, JEOL, Tokyo). Raman spectra were collected *via* a Raman microscope (model R-XploRA Plus, Horiba, Paris, France) with the use of a 638 nm laser. The diffuse reflectance spectra were obtained with a model UV-3600 Plus instrument (Shimadzu, Kyoto, Japan). The photoluminescence and fluorescence decays of the phosphors were recorded on a FP-8600 fluorospectrophotometer (JSACO, Tokyo) with a temperature controller (HPC-836, JSACO) and a liquid nitrogen cooling unit (PMU-830, JSACO). The internal quantum yield (IQY) of the samples was measured using the integrated sphere on the same FP-8600 instrument.

3. Results and discussion

3.1. Crystal structure and microstructure

Fig. 1a shows a detailed crystal structure of LaAlO_3 and the coordination environment of the cations. AlO_6 octahedra are connected with each other by corner-sharing to form the basic framework of LaAlO_3 . The La^{3+} ion is coordinated with twelve oxygen atoms and located in the cavities of eight AlO_6 octahedra. According to the similar ionic radii between Mn^{4+} (0.53 Å, CN = 6) and Al^{3+} (0.535 Å, CN = 6), the luminescence centers of the Mn^{4+} ions would occupy the crystallographic sites of Al^{3+} in the AlO_6 units. Therefore, from consideration of ionic radii, Ti^{4+} (0.605 Å, CN = 6) and Ga^{3+} (0.62 Å, CN = 6) are expected to substitute for Al^{3+} (0.535 Å, CN = 6). Moreover, Ba^{2+} (1.61 Å, CN = 12) and Y^{3+} (1.075 Å, CN = 9) would replace La^{3+} (1.36 Å, CN = 12). Fig. 1b and c show the XRD patterns of the LBAT:0.001 Mn^{4+} ($x = 0-0.25$) and LYAG:0.001 Mn^{4+} ($y = 0-0.25$) samples. Obviously, most of the samples fit well with the standard crystal diffraction data (JCPDS no. 85-0848) of the LaAlO_3

compound. However, when the x - and y -values exceed 0.2, the impurities BaTiO_3 (JCPDS no. 75-2117)²⁰ and $\text{Y}_4\text{Al}_2\text{O}_9$ (JCPDS no. 83-0935)²¹ are yielded, respectively. Therefore, later discussion is based on x - and y -values of no more than 0.2. As seen in Fig. 1b and c, all the diffraction peaks shift to lower angles gradually with increasing x - and y -values. To analyze the shifts in diffraction peak with increasing x - and y -values, enlarged XRD patterns in the range of 32–34° are shown in Fig. 1b and c. The strongest diffraction peak at 33.4° shifts toward lower angles with increasing x - and/or y -value. But the LBAT:0.001 Mn^{4+} ($x = 0-0.2$) samples show a larger shift than that for LYAG:0.001 Mn^{4+} ($y = 0-0.2$) samples. Typically, the average ionic radii of $\text{Ba}^{2+}\text{-Ti}^{4+}$ and $\text{Y}^{3+}\text{-Ga}^{3+}$ pairs are both larger than that of the $\text{La}^{3+}\text{-Al}^{3+}$ pair, and $\text{Ba}^{2+}\text{-Ti}^{4+}$ is the largest among the three pairs. Modulating the $\text{Ba}^{2+}\text{-Ti}^{4+}$ and $\text{Y}^{3+}\text{-Ga}^{3+}$ content in LaAlO_3 :0.001 Mn^{4+} could lead to lattice volume expansion, and the results are in accordance with the experimental data. The dopants entered the crystal structure of LaAlO_3 :0.001 Mn^{4+} successfully, and homogeneous solid solutions were formed. In addition, the diffraction peaks broaden evidently with increasing x - and/or y -value from 0 to 0.2, demonstrating that the crystal lattice becomes imperfect and the distortion degree of the crystal structures increases.²²

In order to further observe the variation of the crystal lattice of LaAlO_3 :0.001 Mn^{4+} after the incorporation of $\text{Ba}^{2+}\text{-Ti}^{4+}$ and $\text{Y}^{3+}\text{-Ga}^{3+}$ pairs, Rietveld refinements were conducted (Fig. S1†). The refinement results for LBAT:0.001 Mn^{4+} ($x = 0-0.2$) and LYAG:0.001 Mn^{4+} ($y = 0-0.2$) samples are summarized in Tables S1 and S2,† respectively. As can be seen, the residual factors (R_{wp} , R_{p} and χ^2) for all the samples converged to low levels, showing that these refinement results are reliable. The lattice constant and the M–O bond length in MO_6 octahedra increase

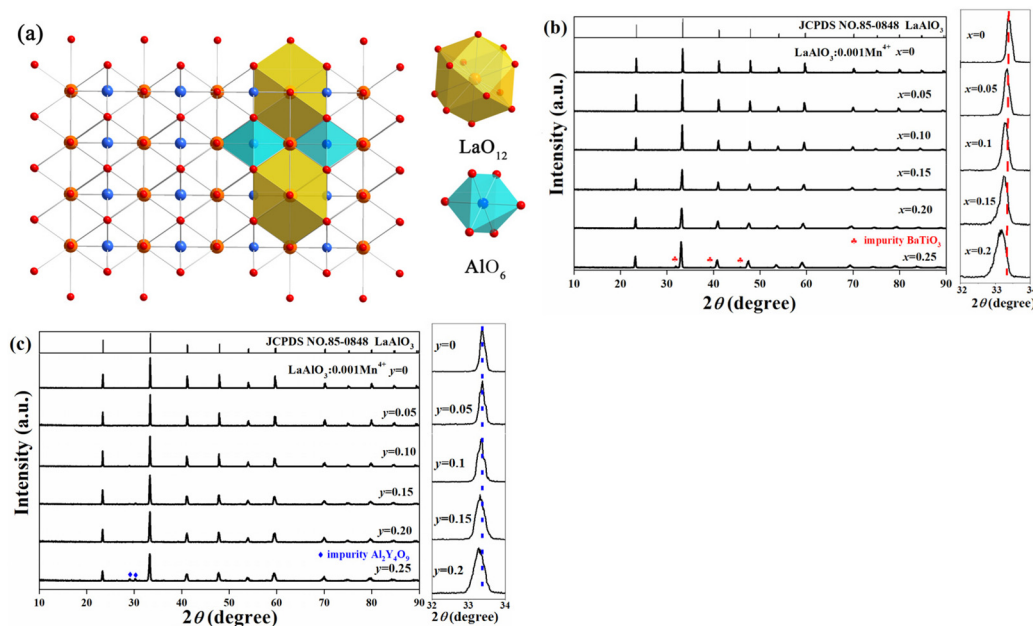


Fig. 1 (a) Crystal structure of LaAlO_3 . XRD patterns of (b) LBAT:0.001 Mn^{4+} ($x = 0-0.25$) and (c) LYAG:0.001 Mn^{4+} ($y = 0-0.25$) in the 2θ range of 10–90° and enlarged XRD patterns in the range of 32–34°.

linearly with increasing the doping content of $\text{Ba}^{2+}\text{-Ti}^{4+}$ and $\text{Y}^{3+}\text{-Ga}^{3+}$ (Fig. 2a and b). The O–M–O bond angle shows a decreasing trend with the increase in the x -value, while it shows a remarkably increasing trend with increasing y -value (Fig. 2c). The octahedral tilting can be reflected by the octahedral tilting angle φ between the Al–O bonding and the coordinated axis, which is the angle deviated by 90.00° .⁷ The increased φ -value shows serious octahedral tilting distortion with $\text{Y}^{3+}\text{-Ga}^{3+}$ co-doping, but the value decreases with increasing x -value, implying that the octahedral tilting distortion is suppressed (Fig. 2d). These variations of the samples co-doped with $\text{Ba}^{2+}\text{-Ti}^{4+}$ and $\text{Y}^{3+}\text{-Ga}^{3+}$ in lattice constant, bond length, bond angle and tilting angle are different from each other, implying that co-doping $\text{Ba}^{2+}\text{-Ti}^{4+}$ and $\text{Y}^{3+}\text{-Ga}^{3+}$ pairs may result in various distortions of the crystal lattice, owing to the mismatch in ionic radii of doping cations and the resultant octahedral tilting degrees.^{23,24} Consequently, the distortions of LBAT:0.001Mn^{4+} ($x = 0.05\text{--}0.2$) samples are caused by the competition between the mismatched ionic radii and the suppression of octahedral tilting. On the contrary, the distortions of LYAG:0.001Mn^{4+} ($x = 0.05\text{--}0.2$) are composed of the mismatched ionic radii and the increased octahedral tilting.

Raman spectra is a useful tool to detect the distortion of LaAlO_3 .^{7,25} Fig. 3a and b display the Raman spectra of LBAT:0.001Mn^{4+} ($x = 0\text{--}0.2$) samples and LYAG:0.001Mn^{4+} ($y = 0\text{--}0.2$) samples, respectively. For the $\text{LaAlO}_3\text{:0.001Mn}^{4+}$ phosphor, two strong peaks at 121 and 152 cm^{-1} are observed,

which are assigned to A_{1g} mode (rotation of the oxygen octahedra) and E_g mode (pure La vibration), respectively. The wavenumber of A_{1g} mode mainly correlates with the tilting angle of the AlO_6 octahedron.¹¹ A blue shift of the A_{1g} wavenumber from 121 to 109 cm^{-1} is detected with increasing the x -value from 0 to 0.2, while a red shift from 121 to 195 cm^{-1} is observed with increasing the y -value from 0 to 0.2. These phenomena explain that introducing $\text{Ba}^{2+}\text{-Ti}^{4+}$ reduces the octahedral tilting, while co-doping with the $\text{Y}^{3+}\text{-Ga}^{3+}$ pair increases the octahedral tilting. The results are consistent with the variations in the tilting angle φ (Fig. 2d). At the same time, the E_g wavenumber at 152 cm^{-1} remains in the same position with increasing the x - or y -value. Because the defects in the crystal structure may contribute to the broadening of the vibrational bands, the full width at half-maximum (FWHM) can reflect the amount of defects.²⁵ The FWHM value of the A_{1g} mode is 15 cm^{-1} for $\text{LaAlO}_3\text{:0.001Mn}^{4+}$, and the value shows a continuous increase with increasing the $\text{Ba}^{2+}\text{-Ti}^{4+}$ and $\text{Y}^{3+}\text{-Ga}^{3+}$ contents. Furthermore, the FWHM value of LYAG:0.001Mn^{4+} ($y = 0.05\text{--}0.2$) is always higher than that of LBAT:0.001Mn^{4+} ($x = 0.05\text{--}0.2$), implying that introducing $\text{Y}^{3+}\text{-Ga}^{3+}$ would generate more serious defects in the crystal structure.

The SEM images, TEM images, HR-TEM lattice fringes and element distributions for $\text{LaAlO}_3\text{:0.001Mn}^{4+}$, $x = 0.2$ and $y = 0.2$ samples are displayed in Fig. 4. The particles are irregular in shape and the sizes are in the range of 1.5–6 μm , which is

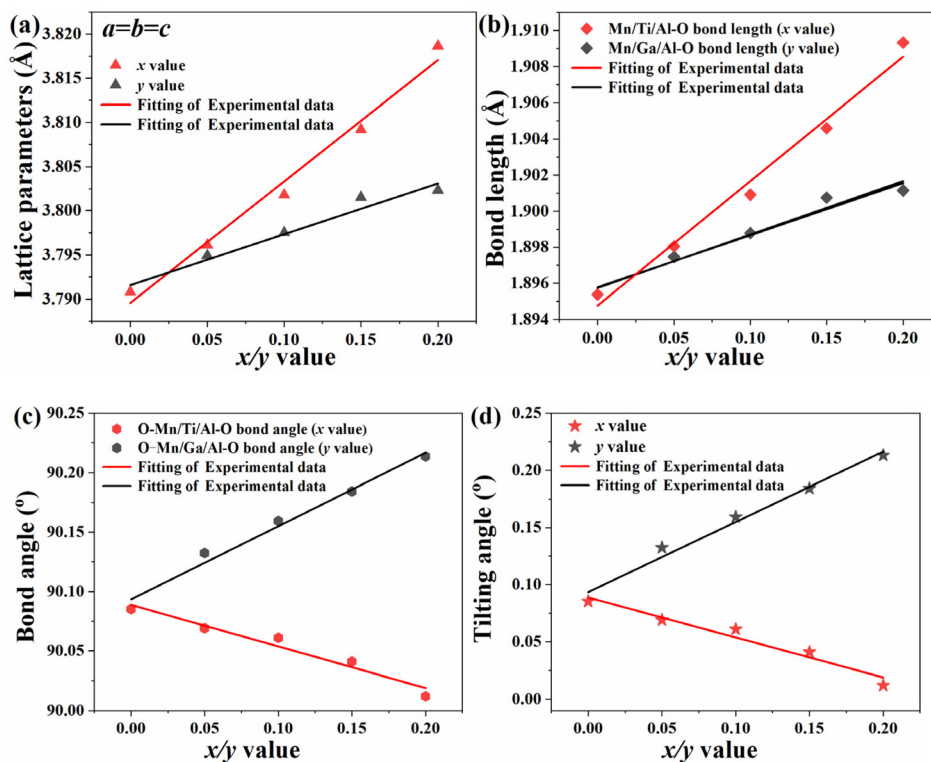


Fig. 2 The variations of (a) cell parameter, (b) bond length, (c) O–M–O bond angle in a MO_6 octahedron and (d) octahedral tilting angle versus various $\text{Ba}^{2+}\text{-Ti}^{4+}$ ($x = 0\text{--}0.2$) and $\text{Y}^{3+}\text{-Ga}^{3+}$ ($y = 0\text{--}0.2$) content doped $\text{LaAlO}_3\text{:0.001Mn}^{4+}$ phosphors based on Rietveld refinement results.

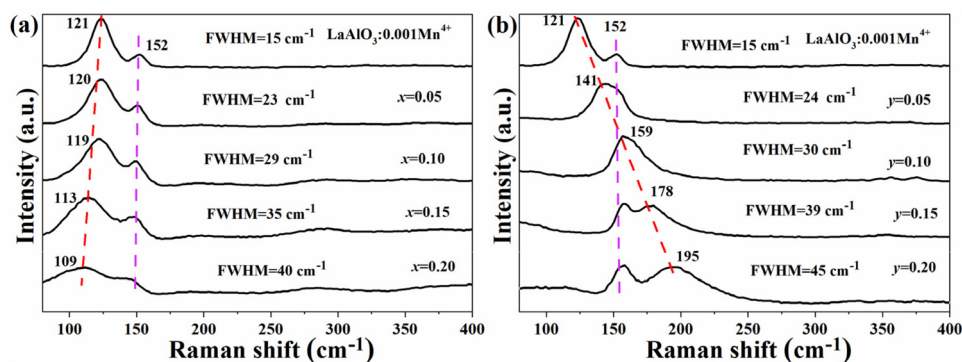


Fig. 3 Raman spectra of (a) LBAT:0.001Mn⁴⁺ ($x = 0-0.20$) and (b) LYAG:0.001Mn⁴⁺ ($y = 0-0.20$).

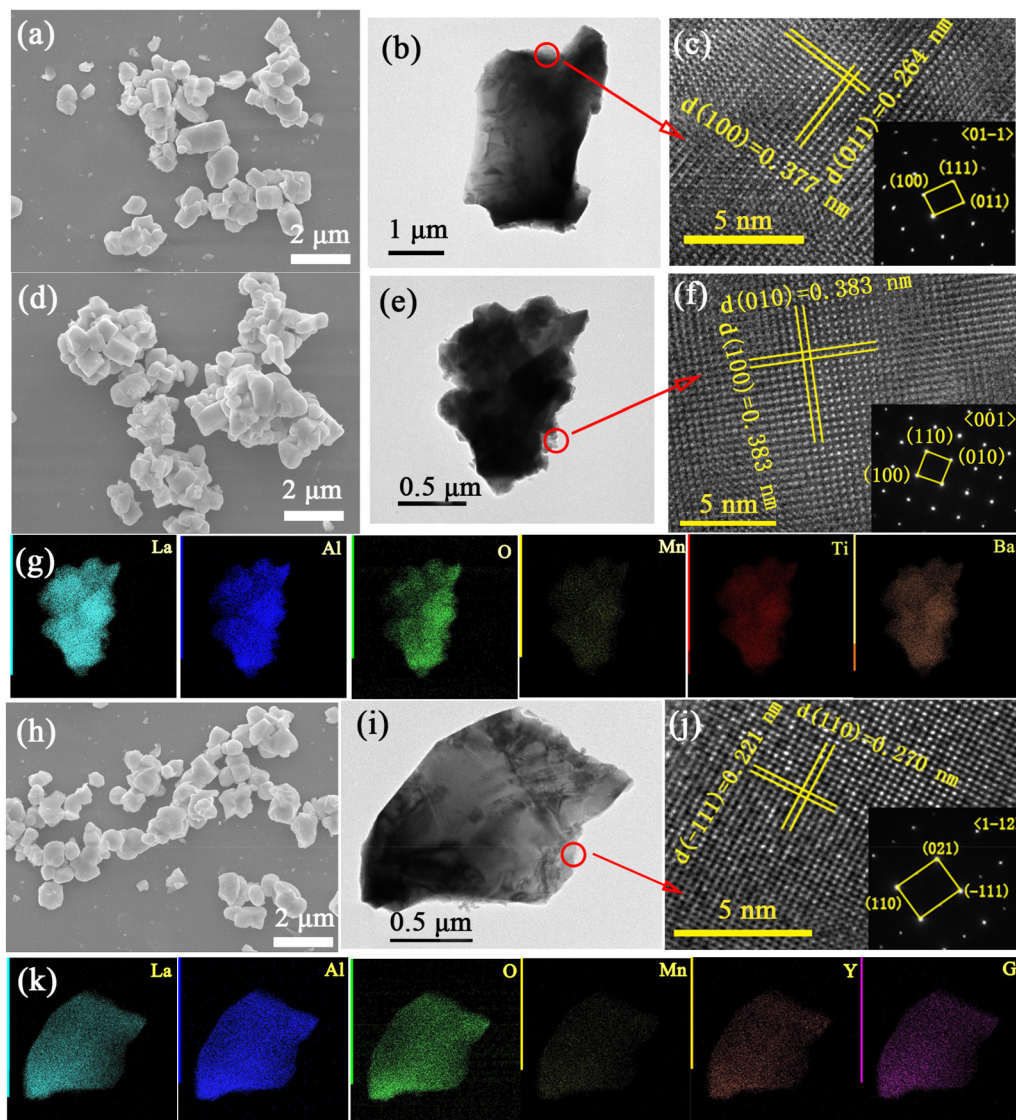


Fig. 4 SEM (a, d, h), TEM images (b, e, i), HR-TEM lattice fringes (c, f, j) and element distribution (g, k) for LaAlO₃:0.001Mn⁴⁺ (a, b, c), $x = 0.2$ (d, e, f, g) and $y = 0.2$ (h, i, g, k).

similar to the particles prepared at higher sintering temperatures.^{26,27} Their surface morphology does not change significantly depending on the different co-doping amounts. The distinct interplanar space fingers indicate high crystallinity of the samples. The d -values corresponding to the (100) and (011) planes are determined to be ~ 0.377 and ~ 0.264 nm for $\text{LaAlO}_3:0.001\text{Mn}^{4+}$ (Fig. 4c). The d -value corresponding to (100) plane is calculated to be ~ 0.383 nm for the $x = 0.2$ sample, and the d -value corresponding to the (011) plane is estimated to be ~ 0.270 nm for the $y = 0.2$ sample. Due to the $\text{Ba}^{2+}\text{-Ti}^{4+}$ and $\text{Y}^{3+}\text{-Ga}^{3+}$ doping contribution to lattice expansion, an increase in the interplanar spacing is found with increasing the x - and y -values. The element mapping of a single particle indicates a uniform distribution of La, Al, O, Mn, Ba and Ti (Y and Ga) for the $x = 0.2$ ($y = 0.2$) sample (Fig. 4g and k). After the comparative analysis, the optimal phosphor samples $\text{LBAT}:0.001\text{Mn}^{4+}$ and $\text{LYAG}:0.001\text{Mn}^{4+}$ were successfully synthesized.

3.2. Photoluminescence of $\text{LBAT}:0.001\text{Mn}^{4+}$ and $\text{LYAG}:0.001\text{Mn}^{4+}$ samples

Fig. 5a reveals the diffuse reflection spectra of $\text{LaAlO}_3:0.001\text{Mn}^{4+}$, $x = 0.2$ and $y = 0.2$ samples. All of the samples exhibit three strong and wide absorption bands from 240 to 550 nm, which correspond to the strong spin-allowed transition of Mn^{4+} from ${}^4\text{A}_{2g}$ to the excited levels ${}^4\text{T}_{1g}$, ${}^2\text{T}_{2g}$ and ${}^4\text{T}_{2g}$. But a strong band at ~ 280 nm related to the $\text{Mn}^{4+}\text{-O}^{2-}$ charge-transfer band is only observed for the $\text{LaAlO}_3:0.001\text{Mn}^{4+}$ and $\text{LYAG}:0.001\text{Mn}^{4+}$ samples. For the purpose of gaining more information about the band structures of the above materials, the optical band gaps (E_g) were determined for the LaAlO_3 , $\text{La}_{0.8}\text{Ba}_{0.2}\text{Al}_{0.8}\text{Ti}_{0.2}\text{O}_3$ and $\text{La}_{0.8}\text{Y}_{0.2}\text{Al}_{0.8}\text{Ga}_{0.2}\text{O}_3$ hosts. The corresponding equation was used as follows:^{28–30}

$$(\alpha h\nu)^n = A(h\nu - E_g) \quad (1)$$

where α , h , ν , and A represent the absorption coefficient, Planck constant, frequency and constant, respectively. n stands

for the direct or indirect transition while it is equal to 2 or $\frac{1}{2}$, respectively. According to the previous report,³¹ the band structure of LaAlO_3 is indirect. As shown in Fig. 5b, based on the plot of $(\alpha h\nu)^{1/2}$ vs. $h\nu$, the E_g for LaAlO_3 , $\text{La}_{0.8}\text{Ba}_{0.2}\text{Al}_{0.8}\text{Ti}_{0.2}\text{O}_3$ and $\text{La}_{0.8}\text{Y}_{0.2}\text{Al}_{0.8}\text{Ga}_{0.2}\text{O}_3$ is estimated to be 5.6, 3.9 and 5.7 eV, respectively. The $\text{Ba}^{2+}\text{-Ti}^{4+}$ doping induces the large decrease in the E_g value. For further analysis, the changes in E_g , the band structure and the partial densities of states (DOS) for $\text{La}_{0.8}\text{Ba}_{0.2}\text{Al}_{0.8}\text{Ti}_{0.2}\text{O}_3$ were analyzed by density functional theory (DFT) calculation (Fig. S2†). The band structure and DOS of LaAlO_3 were mentioned in our previous work, and the E_g value is 5.0 eV.³¹ Furthermore, the La orbital levels dominantly contribute to the conduction band minimum (CBM), while the O orbital levels correspond to the valence band maximum (VBM). However, for the $\text{La}_{0.8}\text{Ba}_{0.2}\text{Al}_{0.8}\text{Ti}_{0.2}\text{O}_3$ host, the E_g value is 3.0 eV (Fig. S2a†), which is much smaller than that for LaAlO_3 . This is mainly due to the electronic structure of CBM originating from the Ti orbital levels predominantly, with the VBM still arising from the O orbital levels (Fig. S2b†). It is noteworthy that there is a distinct smaller E_g of 3.0 eV for $\text{La}_{0.8}\text{Ba}_{0.2}\text{Al}_{0.8}\text{Ti}_{0.2}\text{O}_3$, confirming that $\text{Ba}^{2+}\text{-Ti}^{4+}$ doping reduces the bandgap. The results match well with the experimental data. Therefore, co-doping $\text{Ba}^{2+}\text{-Ti}^{4+}$ in LaAlO_3 leads to significant changes in E_g , and may affect the luminescence properties of Mn^{4+} .

To investigate the effects of $\text{Ba}^{2+}\text{-Ti}^{4+}$ and $\text{Y}^{3+}\text{-Ga}^{3+}$ chemical unit doping on the luminescence of Mn^{4+} , the photoluminescence excitation (PLE) and photoluminescence (PL) spectra of $\text{LBAT}:0.001\text{Mn}^{4+}$ ($x = 0\text{--}0.2$) and $\text{LYAG}:0.001\text{Mn}^{4+}$ ($y = 0\text{--}0.2$) were measured and the results are shown in Fig. 6. There are two characteristic excitation bands that appear when monitored at 726 nm for $\text{LaAlO}_3:0.001\text{Mn}^{4+}$. The peak at 340 nm is assigned to the overlap of the $\text{Mn}^{4+}\text{-O}^{2-}$ charge-transfer band and ${}^4\text{A}_{2g}\text{-}{}^4\text{T}_{1g}$ and ${}^4\text{A}_{2g}\text{-}{}^2\text{T}_{2g}$ transitions, while the other peak at ~ 490 nm is related to the ${}^4\text{A}_{2g}\text{-}{}^4\text{T}_{2g}$ transition. There is an obvious red shift in the excitation spectra for $\text{LBAT}:0.001\text{Mn}^{4+}$ ($x = 0\text{--}0.2$) from ~ 333 to ~ 356 nm. The shift for $\text{LYAG}:0.001\text{Mn}^{4+}$ ($y = 0\text{--}0.2$) is from ~ 333 to ~ 358 nm. Furthermore, the peak at ~ 280 nm disappears for

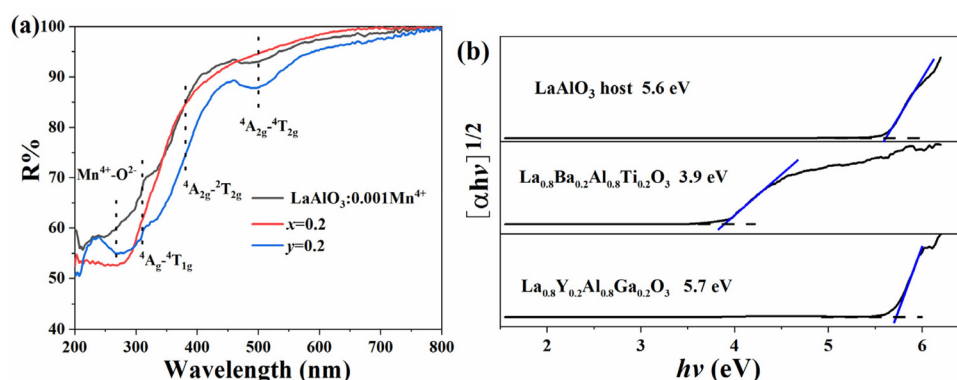


Fig. 5 (a) The diffuse reflection spectra of $\text{LaAlO}_3:0.001\text{Mn}^{4+}$, $x = 0.2$ and $y = 0.2$ samples. (b) The band gap energy determination for the selected hosts.

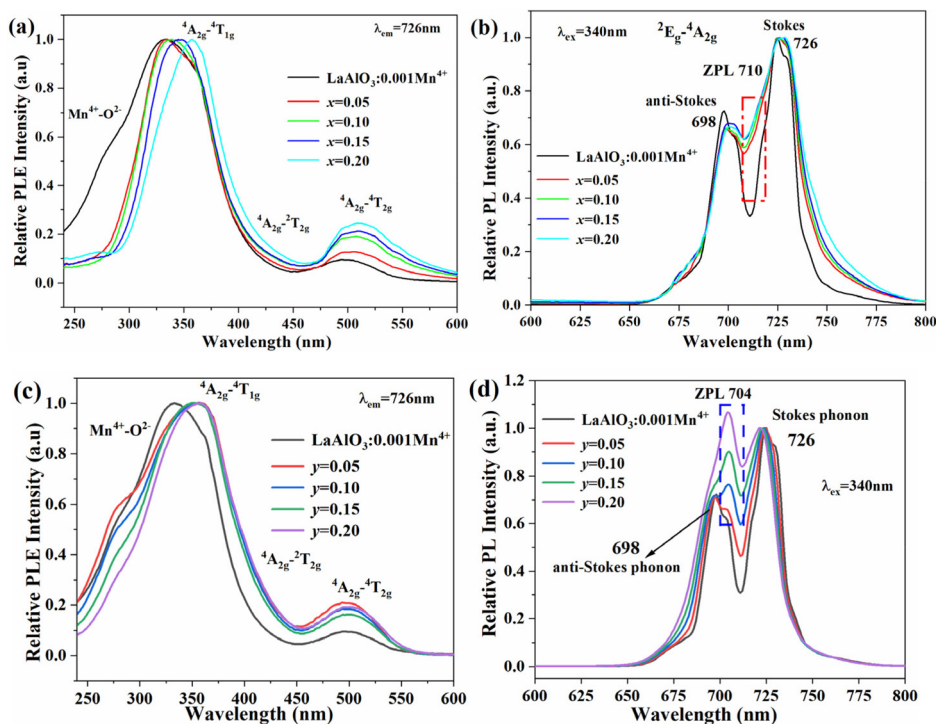


Fig. 6 PLE (a and c) and PL (b and d) spectra for (a and b) LBAT:0.001Mn⁴⁺ ($x = 0-0.2$) and (c and d) LYAG:0.001Mn⁴⁺ ($y = 0-0.2$) at room temperature.

LBAT:0.001Mn⁴⁺ ($x = 0.05-0.2$), while the PLE spectra of the LYAG:0.001Mn⁴⁺ ($y = 0.05-0.2$) samples keep the original shape. The appearance is due to the change of the optical band gap, which will be discussed in later. Under 340 nm excitation, the PL spectrum of LaAlO₃:0.001Mn⁴⁺ is composed of two bands, including the anti-Stokes phonon band at 698 nm and Stokes phonon band at 726 nm of the ²E_g-⁴A_{2g} transition. The zero-phonon line (ZPL) emission is too low in intensity to be detected. With the introduction of Ba²⁺-Ti⁴⁺ and Y³⁺-Ga³⁺, both peaks remain at the same position and the shape persists. However, a big difference between the anti-Stokes phonon band and the Stokes phonon band is found. A new peak at 710 or 704 nm was generated by co-doping Ba²⁺-Ti⁴⁺ and Y³⁺-Ga³⁺ in LaAlO₃:0.001Mn⁴⁺, and accordingly, the two divided peaks became a broad band. The new peak is related to the ZPL emission. Through the co-substitution of Ba²⁺-Ti⁴⁺, the new peak at 710 nm is enhanced slowly, while an unusual improvement in the peak at 704 nm is obtained by increasing the Y³⁺-Ga³⁺ content. Thus, due to the different ZPL energies and intensities, the PL shape of these phosphors shows a huge difference by co-doping different cation pairs.

As is generally known, the emission of Mn⁴⁺ is mainly dominated by the vibration of the side bands. In order to observe the variations of the ZPL in detail, the vibration of the side bands should be suppressed. Here, the high-resolution PLE and PL spectra of these samples were recorded at low temperature (77 K), as shown in Fig. 7. The excitation spectra

are similar to the spectra measured at room temperature for the LBAT:0.001Mn⁴⁺ ($x = 0-0.2$) and LYAG:0.001Mn⁴⁺ ($y = 0-0.2$) samples. The PLE spectrum of LaAlO₃:0.001Mn⁴⁺ is fitted into four bands located at 316, 347, 410 and 490 nm, which correspond to the Mn⁴⁺-O²⁻ charge-transfer band, and ⁴A_{2g}-⁴T_{1g}, ⁴A_{2g}-²T_{2g} and ⁴A_{2g}-⁴T_{2g} transitions of Mn⁴⁺. For the LBAT:0.001Mn⁴⁺ ($x = 0.05-0.2$) phosphors, the PLE spectra can be well divided into three sub-bands, which are assigned to the ⁴A_{2g}-⁴T_{1g}, ⁴A_{2g}-²T_{2g} and ⁴A_{2g}-⁴T_{2g} transitions of Mn⁴⁺. However, the PLE spectra of LYAG:0.001Mn⁴⁺ ($y = 0.05-0.2$) phosphors are well decomposed into four peaks, which are similar to the LaAlO₃:0.001Mn⁴⁺ sample. Both ⁴A_{2g}-⁴T_{1g} and ⁴A_{2g}-⁴T_{2g} transition peaks show red shifts for the LBAT:0.001Mn⁴⁺ ($x = 0-0.2$) and LYAG:0.001Mn⁴⁺ ($y = 0-0.2$) phosphors. Notably, under the excitation of 340 nm, the Stokes peak is still at 726 nm and the anti-Stokes peak disappears at 77 K. According to the previous work, the red shift of Mn⁴⁺ excitation peaks is mainly due to the change in the crystal field strength (D_q). D_q could be estimated by the following equation:¹⁶

$$D_q = \frac{Ze^2r^4}{6R^5} \quad (2)$$

where Z stands the charge or valence of the anion, and r and R represent the radius of the d wave function and the bond length between the Mn⁴⁺ and its ligands, respectively. In LBAT:0.001Mn⁴⁺ ($x = 0.05-0.2$) and LYAG:0.001Mn⁴⁺ ($y = 0.05-0.2$) phosphors, the average bond length of Mn-O is

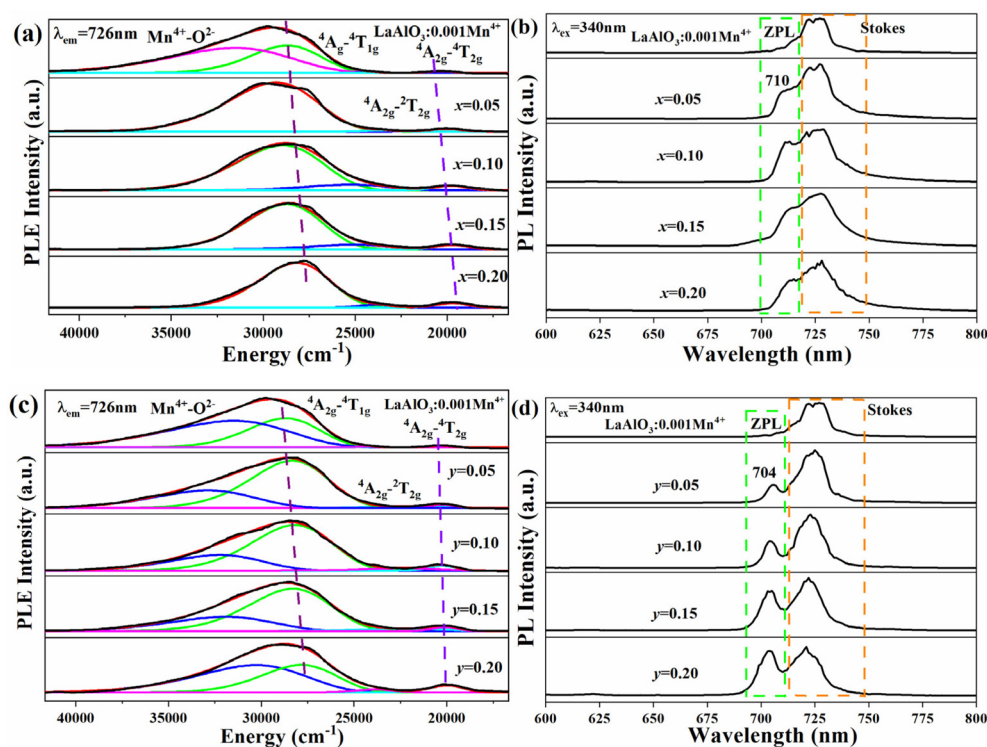


Fig. 7 PLE (a and c) and PL (b and d) spectra for (a and b) LBAT:0.001Mn⁴⁺ ($x = 0-0.2$) and (c and d) LYAG:0.001Mn⁴⁺ ($y = 0-0.2$) at 77 K.

larger than that in LaAlO₃:0.001Mn⁴⁺ (Fig. 2b). Therefore, a larger R can lead to a smaller D_q value, and it results in a red shift of the excitation peak with increasing x - and y -values. According to the Tanabe–Sugano energy level diagram, it can be seen that the ²E_g and ⁴A_{2g} energy levels are almost parallel to the horizontal ordinate.¹² Thus, the ²E_g and ⁴A_{2g} energy levels are not affected by changing D_q , further implying that the emission energy is basically independent of the D_q .

Notably, the ZPL emission peak appears by co-doping Ba²⁺–Ti⁴⁺ and Y³⁺–Ga³⁺, but the positions and the intensities of the ZPL band are significantly different. For the LaAlO₃:0.001Mn⁴⁺ sample, the ZPL emission peak is too low to observe. Based on previous work, the ZPL in LaAlO₃:Mn⁴⁺ is located at ~710 nm.¹⁵ Introducing Ba²⁺–Ti⁴⁺ to replace La³⁺–Al³⁺ results in the appearance of the ZPL at 710 nm, the intensity of which increases slowly with the increase in x . However, for the LYAG:0.001Mn⁴⁺ ($y = 0.05-0.2$) phosphors, the position of the ZPL is at 704 nm, which displays a blue shift compared with that for the LaAlO₃:Mn⁴⁺ sample, and the ZPL intensity increases with a further increase in the y value. Fig. 8a shows the intensity ratio of the ZPL to the total emission. The intensity and energy of the ZPL, which are related to the emission without the participation of any phonons, are only dependent on the host lattice. Compared with the phonon sidebands, the ZPL is much more sensitive to the local coordination structure. The intensity is determined by the local symmetry around Mn⁴⁺.³² With the substitution of Ba²⁺–Ti⁴⁺ for La³⁺–Al³⁺, the local symmetry of Mn⁴⁺ changes a little due to the competition of the increase in bond distances and the suppression of octa-

hedral tilting, and thus the intensity of the ZPL shows a slow increase. However, when co-doping Y³⁺–Ga³⁺, owing to the increase in bond distances and octahedral tilting, the local symmetry of Mn⁴⁺ in LYAG:0.001Mn⁴⁺ ($y = 0.05-0.2$) decreases gradually, which thus contributes to an enhanced ZPL intensity. In fact, the emission energy of Mn⁴⁺ corresponds to the hybridization, which is related to the Mn–O bond length and O–Mn–O bond angle.¹⁸ A longer Mn–O bond length and larger O–Mn–O bond angle distortion generally lead to a smaller Mn–O hybridization, and then contribute to higher emission energies.^{18,19} According to the XRD Rietveld refinement information, LYAG:0.001Mn⁴⁺ ($y = 0.05-0.2$) samples show a shorter Mn–O bond length compared with that for LBAT:0.001Mn⁴⁺ ($x = 0.05-0.2$), but they exhibit larger O–Mn–O bond angle distortion. Actually, the ZPL emission energies for LYAG:0.001Mn⁴⁺ samples are higher than those of LBAT:0.001Mn⁴⁺. Thus, through considering the influence of two aspects, the results show that octahedral tilting distortion, which affects the serious O–Mn–O bond angle distortion, is more important for the ZPL energy of Mn⁴⁺ in perovskite oxides.

Generally, a long decay time is obtained for luminescence centers in a symmetrical surrounding, while a short decay time is observed when the luminescence centers are located in the distorted site.³³ Fig. S3 and S4† show the fluorescence decay curves corresponding to Mn⁴⁺ in the LBAT:0.001Mn⁴⁺ ($x = 0-0.2$) and LYAG:0.001Mn⁴⁺ ($y = 0-0.2$) phosphors under excitation at 340 nm, as monitored at 726 nm at room temperature and at 77 K. All decay curves are found to be well fitted by a single exponential function, suggesting the single site occu-

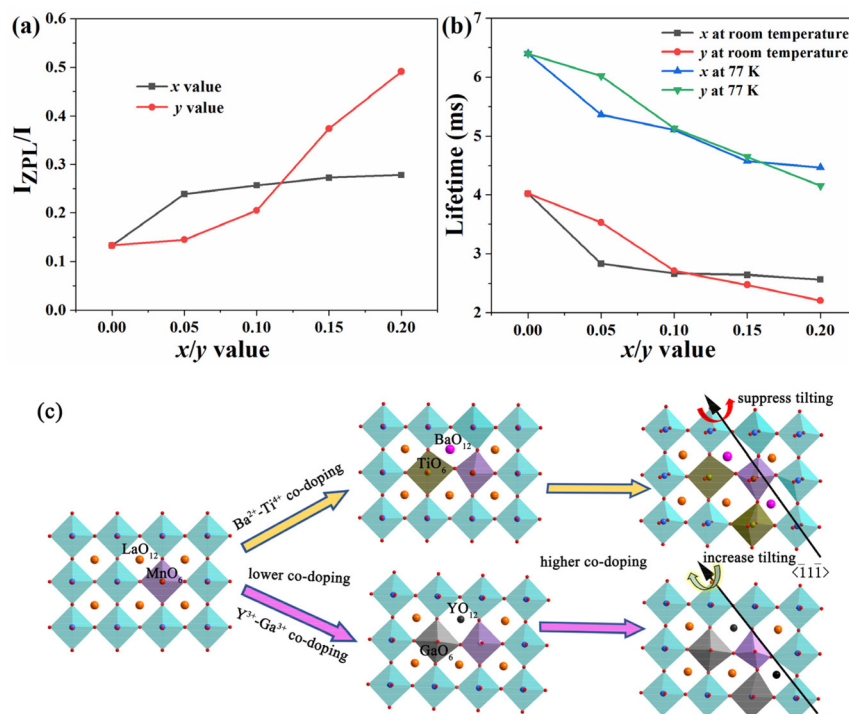


Fig. 8 (a) Related intensity ratio between ZPL and total emission. (b) The variation trend of lifetime at room temperature and 77 K with increasing x - and y -values. (c) Structural distortion trend of the MnO_6 octahedron with different doping amounts.

pancy of the Mn^{4+} in the host lattice. It is expressed as follows:³⁴

$$I_t = I_0 + A_{\text{exp}} \left(\frac{-t}{\tau} \right) \quad (3)$$

where I_t and I_0 are the luminescence intensities at time t and 0. A refers to a constant and τ represents the exponential component of the decay time. The lifetime decreases with the addition of $Ba^{2+}-Ti^{4+}$ and $Y^{3+}-Ga^{3+}$. Furthermore, the decrease trend is rapid for LYAG:0.001 Mn^{4+} ($y = 0-0.2$) phosphors whether at room temperature or at 77 K, compared to that for LBAT:0.001 Mn^{4+} ($x = 0-0.2$) samples (Fig. 8b). These results are identical to the ZPL intensity variations.

Through the above analysis, the energy and intensity of ZPL emission peak are tightly related to the Mn^{4+} local structure environment, the same as the decay time. Fig. 8c shows the structural distortion trend of the MnO_6 octahedron with different doping types and amounts. When Mn^{4+} is incorporated into the $LaAlO_3$ host, Mn^{4+} is surrounded by six coordinated O^{2-} ions to form a MnO_6 octahedron. The MnO_6 octahedron connects with AlO_6 octahedra and LaO_{12} polyhedrons, and Mn^{4+} is located in a high-symmetry surrounding environment, leading to a low ZPL intensity and the longest lifetime among all the phosphors. With $Ba^{2+}-Ti^{4+}$ substitution, some O^{2-} vertices of the MnO_6 octahedron would link to Ba^{2+} and Ti^{4+} , inducing a change in Mn–O bond length due to the mismatched cation size. However, a reduction of octahedral tilting also takes place with increasing the x -value, which

makes the MnO_6 more symmetrical. The Mn–O bond lengths and O–M–O bond angles are determined by the two factors. Higher level substitution of $Ba^{2+}-Ti^{4+}$ contributes to a growing number of BaO_{12} and TiO_6 distributed around MnO_6 , but the degree of Mn^{4+} symmetry is almost constant. Thus, the intensity of ZPL increases slowly and the lifetime decreases slowly, owing to the small change of the local symmetry of Mn^{4+} . On the contrary, with the chemical unit co-substitution of $Y^{3+}-Ga^{3+}$ for $La^{3+}-Al^{3+}$, the distortions consist of the cation size mismatch and the increased octahedral tilting. The increased octahedral tilting would make Mn^{4+} be in a more asymmetrical local environment with increasing the y -value. Therefore, the ZPL intensity increases quickly and the lifetime decreases linearly with increasing the y -value. Notably, when a small amount is added, the ZPL intensity for LBAT:0.001 Mn^{4+} ($x = 0.05, 0.1$) is higher than that for LYAG:0.001 Mn^{4+} ($y = 0.05, 0.1$) and the lifetime for LBAT:0.001 Mn^{4+} ($x = 0.05, 0.1$) is shorter than that for LYAG:0.001 Mn^{4+} ($y = 0.05, 0.1$). This is because the average ionic radius of $Ba^{2+}-Ti^{4+}$ is larger than that of the $Y^{3+}-Ga^{3+}$ pair, and so the distortions arising from cation size mismatch were initially dominant. But the LYAG:0.001 Mn^{4+} ($y = 0.15, 0.2$) phosphors show a higher ZPL intensity and shorter decay time, compared to LBAT:0.001 Mn^{4+} ($x = 0.15, 0.2$) phosphors, because the octahedral tilting takes the dominant role at higher doping contents.

Fig. 9 displays the mechanisms in $LaAlO_3:0.001Mn^{4+}$, $x = 0.2$ and $y = 0.2$ samples for a clear description of the energy transition process. For $LaAlO_3:0.001Mn^{4+}$ and $y = 0.2$, the electron is excited from the ${}^4A_{2g}$ energy level to ${}^4T_{1g}$, ${}^2T_{2g}$, ${}^4T_{2g}$ and

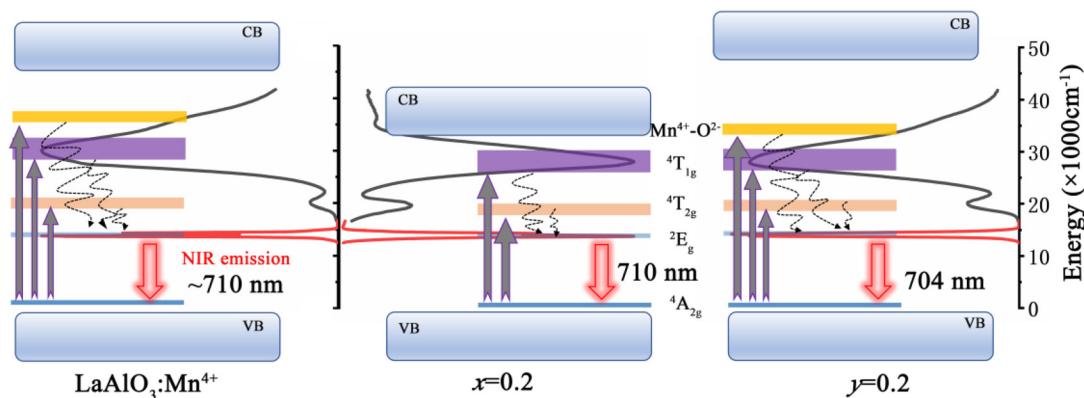


Fig. 9 Mechanisms of luminescence in $\text{LaAlO}_3:0.001\text{Mn}^{4+}$, $x = 0.2$ and $y = 0.2$ samples.

even the $\text{Mn}^{4+}-\text{O}^{2-}$ charge-transfer band. However, the observation is different from that for the $x = 0.2$ sample. Because the conduction band bottom shifts down and then draws the $\text{Mn}^{4+}-\text{O}^{2-}$ level, the excited electron jumps to the conduction band directly, rather than the $\text{Mn}^{4+}-\text{O}^{2-}$ level. So the $\text{LaAlO}_3:0.001\text{Mn}^{4+}$ ($x = 0.05-0.2$) phosphors do not show the $\text{Mn}^{4+}-\text{O}^{2-}$ charge transfer band in excitation spectra. Then the excited electrons relax to the ${}^2\text{E}_g$ level by a non-radiative transition process and finally transfer to the ${}^4\text{A}_{2g}$ energy level with the output of near-infrared emission. According to the PLE spectra (Fig. 6a and c), the samples co-doped by $\text{Ba}^{2+}-\text{Ti}^{4+}$ and

$\text{Y}^{3+}-\text{Ga}^{3+}$ have lower energy in the ${}^4\text{T}_{1g}$, ${}^4\text{T}_{2g}$ states, which results in a red shift of the excitation peak. At the same time, the Stokes and anti-Stokes emissions are kept at the same positions, but only the energy of the ZPL emission changes, which is clearly described in Fig. 9.

Moreover, the internal quantum yield (IQY) for $\text{LaAlO}_3:0.001\text{Mn}^{4+}$ has been estimated to be 72.5%. For $\text{Ba}^{2+}-\text{Ti}^{4+}$ co-doping, the IQY of the series $\text{LaAlO}_3:0.001\text{Mn}^{4+}$ ($x = 0.05-0.2$) phosphors was analyzed to be 66.7% ($x = 0.05$), 62.4% ($x = 0.1$), 59.3% ($x = 0.15$) and 55.8% ($x = 0.2$), respectively. For $\text{Y}^{3+}-\text{Ga}^{3+}$ co-doping, the IQY of the series

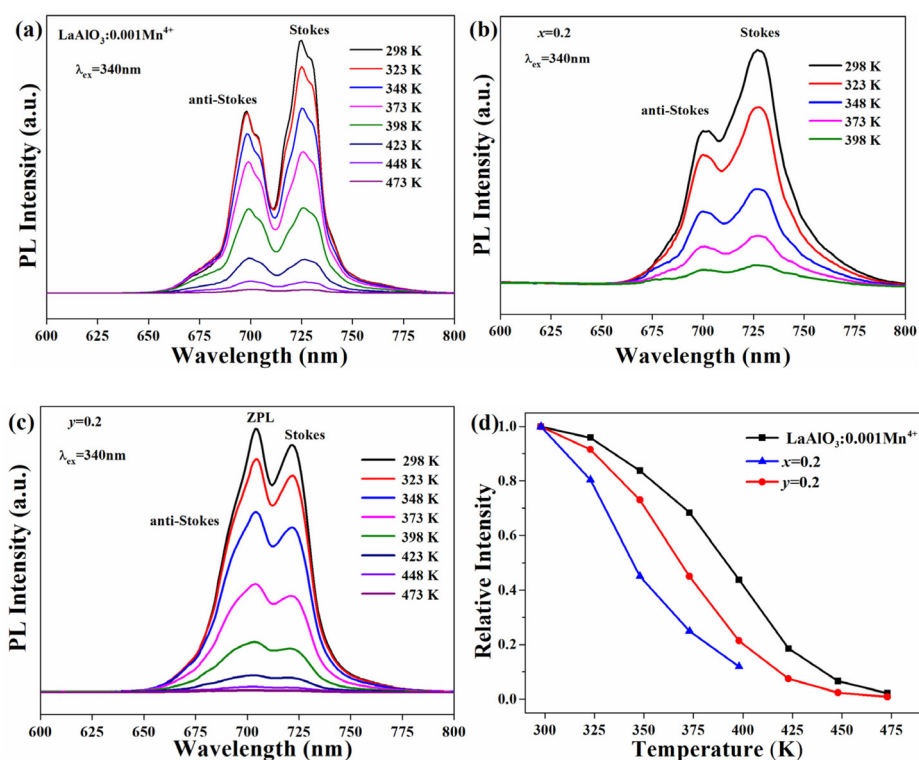


Fig. 10 Temperature-dependent PL spectra of (a) $\text{LaAlO}_3:0.001\text{Mn}^{4+}$, (b) $x = 0.2$ and (c) $y = 0.2$ phosphors. (d) The relative integrated intensity of the three samples.

LYAG:0.001Mn⁴⁺ ($y = 0.05-0.2$) was analyzed to be 70.0% ($y = 0.05$), 67.1% ($y = 0.1$), 63.9% ($x = 0.15$) and 61.3% ($x = 0.2$), respectively. The decreased IQY with increasing x - or y -values is mainly due to the lattice expansion, which induces stronger photon-phonon interaction.³⁵

The temperature-dependent luminescence quenching property is essential to evaluate the thermal stability of phosphors.³⁶⁻³⁸ The temperature luminescent properties were studied in the temperature range of 298–473 K. The temperature-dependent PL spectra of LaAlO₃:0.001Mn⁴⁺, $x = 0.2$ and $y = 0.2$ phosphors are demonstrated in Fig. 10a–c. The relative integral emission intensity of the above three samples is plotted in Fig. 10d. The integral intensity of all the samples decreases monotonically. However, the three samples show different degrees of luminescence quenching with increasing temperature. For better understanding of the thermal quenching behavior, the Arrhenius equation is used to estimate the activation energy (E_a):³⁹

$$I_t = \frac{I_0}{1 + A_{\text{exp}}\left(-\frac{E_a}{kT}\right)} \quad (4)$$

where I_0 and I_t are the emission intensities at the initial temperature and working temperature T , respectively. A is a constant and k represents the Boltzmann constant (8.617×10^{-5} eV K⁻¹). Linear fitting is conducted and the slope is the value of E_a (Fig. S5†). The values are ~0.598, ~0.498 and ~0.583 eV for the LaAlO₃:0.001Mn⁴⁺, $x = 0.2$ and $y = 0.2$ samples, falling into the range of the reported values of Mn⁴⁺-doped oxides.¹⁶

4. Conclusion

A series of La_{1-x}Ba_xAl_{1-x}Ti_xO₃:0.001Mn⁴⁺ (LBAT:0.001Mn⁴⁺, $x = 0-0.25$) and La_{1-y}Y_yAl_{1-y}Ga_yO₃:0.001Mn⁴⁺ (LYAG:0.001Mn⁴⁺, $y = 0-0.25$) samples were successfully synthesized. The substitution of Ba²⁺-Ti⁴⁺ and Y³⁺-Ga³⁺ for La³⁺-Al³⁺ contributed to the increase in the lattice constant and M-O bond length. Furthermore, co-doping Ba²⁺-Ti⁴⁺ resulted in the suppression of octahedral tilting. However, more serious octahedral tilting was found for the Y³⁺-Ga³⁺ substitution. Thus, the distortions of LBAT:0.001Mn⁴⁺ ($x = 0.05-0.2$) samples are caused by the competition between the mismatched ionic radii and the suppression of octahedral tilting. On the contrary, the distortions of LYAG:0.001Mn⁴⁺ ($x = 0.05-0.2$) are composed of the mismatched ionic radii and the increased octahedral tilting. The distortions have a significant influence on the Mn⁴⁺ luminescence. Longer Mn-O bond length induces weaker excitation energy through decreasing D_q for LBAT:0.001Mn⁴⁺ and LYAG:0.001Mn⁴⁺ phosphors. But the various D_q could not change the position of the emission peak. In fact, the emission shape and energy, particularly the ZPL emission, exhibited big changes with co-doping Ba²⁺-Ti⁴⁺ and Y³⁺-Ga³⁺. The ZPL intensity increases with substituting Ba²⁺-Ti⁴⁺ and Y³⁺-Ga³⁺ for La³⁺-Al³⁺. Because the symmetry around Mn⁴⁺ decreases more slowly with co-doping Ba²⁺-Ti⁴⁺ than with co-doping Y³⁺-Ga³⁺,

the intensity of the ZPL for LBAT:0.001Mn⁴⁺ increases more slowly than that in LYAG:0.001Mn⁴⁺. At the same time, the ZPL energy for LBAT:0.001Mn⁴⁺ is higher than that for LYAG:0.001Mn⁴⁺, owing to the larger distortion of the O-Mn-O bond angle.

Conflicts of interest

There are no conflicts to declare.

Acknowledgements

This work was supported in part by the Natural Science Foundation of Liaoning Province (grant 2020-MS-081) and National Natural Science Foundation of China (grants 51302032, 51972047, 52172112).

References

- 1 Y. N. Zheng, R. Z. Zhang, L. Zhang, Q. F. Gu and Z.-A. Qiao, A resol-assisted cationic coordinative co-assembly approach to mesoporous ABO₃ perovskite oxides with rich oxygen vacancy for enhanced hydrogenation of furfural to furfuryl alcohol, *Angew. Chem., Int. Ed.*, 2021, **60**, 4774–4781.
- 2 J. F. Zhao, J. C. Gao, W. M. Li, Y. T. Qian, X. D. Shen, X. Wang, X. Shen, Z. W. Hu, C. Dong, Q. Z. Huang, L. P. Cao, Z. Li, J. Zhang, C. W. Ren, L. Duan, Q. Q. Liu, R. C. Yu, Y. Ren, S.-C. Weng, H.-J. Lin, C.-T. Chen, L.-H. Tjeng, Y. Long, Z. Deng, J. L. Zhu, X. C. Wang, H. M. Weng, R. Z. Yu, M. Greenblatt and C. Q. Jin, A combinatory ferroelectric compound bridging simple ABO₃ and A-site-ordered quadruple perovskite, *Nat. Commun.*, 2021, **12**, 747.
- 3 W. R. Geng, X. W. Guo, Y. L. Zhu, Y. J. Wang, Y. L. Tang, M. J. Han, Y. P. Feng, M. J. Zou, B. Wu, J. Y. Ma, W. T. Hu and X. L. Ma, Oxygen octahedral coupling mediated ferroelectric-antiferroelectric phase transition based on domain wall engineering, *Acta Mater.*, 2020, **198**, 145–152.
- 4 R. Huang, H.-C. Ding, W.-I. Liang, Y.-C. Gao, X.-D. Tang, Q. He, C.-G. Duan, Z. Q. Zhu, J. H. Chu, C. A. J. Fisher, T. Hirayama, Y. Ikuhara and Y.-H. Chu, Atomic-scale visualization of polarization pinning and relaxation at coherent BiFeO₃/LaAlO₃ interfaces, *Adv. Funct. Mater.*, 2014, **24**, 793–799.
- 5 W. L. Lu, P. Yang, W. D. Song, G. M. Chow and J. S. Chen, Control of oxygen octahedral rotations and physical properties in SrRuO₃ films, *Phys. Rev. B: Condens. Matter Mater. Phys.*, 2013, **88**, 214115.
- 6 H. J. Xiang, M. Guennou, J. Íñiguez, J. Kreisel and L. Bellaiche, Rules and mechanisms governing octahedral tilts in perovskites under pressure, *Phys. Rev. B*, 2017, **96**, 054102.

- 7 Y. C. Ji, P. Zhang, L. Q. He, D. Wang, H. Y. Luo, K. Otsuka, Y. Z. Wang and X. B. Ren, Tilt strain glass in Sr and Nb co-doped LaAlO₃ ceramics, *Acta Mater.*, 2019, **168**, 250–260.
- 8 A. Biswas, C.-H. Yang, R. Ramesh and Y. H. Jeong, Atomically flat single terminated oxide substrate surfaces, *Prog. Surf. Sci.*, 2017, **92**, 117–141.
- 9 S. A. Hayward, F. D. Morrison, S. A. T. Redfern, E. K. H. Salje, J. F. Scott, K. S. Knight, S. Tarantino, A. M. Glazer, V. Shuvaeva, P. Daniel, M. Zhang and M. A. Carpenter, Transformation processes in LaAlO₃: neutron diffraction, dielectric, thermal, optical, and raman studies, *Phys. Rev. B: Condens. Matter Mater. Phys.*, 2005, **72**, 054110.
- 10 P. Bouvier and J. Kreisel, Pressure-induced phase transition in LaAlO₃, *J. Phys.: Condens. Matter*, 2002, **14**, 3981–3991.
- 11 M. V. Abrashev, A. P. Litvinchuk, M. N. Iliev, R. L. Meng, V. N. Popov, V. G. Ivanov, R. A. Chakalov and C. Thomsen, Comparative study of optical phonons in the rhombohedrally distorted perovskites LaAlO₃ and LaMnO₃, *Phys. Rev. B: Condens. Matter Mater. Phys.*, 1999, **59**, 4146–4153.
- 12 S. Y. Li, Q. Zhu, X. D. Sun and J.-G. Li, Magical polyhedral twist via chemical unit co-substitution in LaAlO₃:Mn⁴⁺ to greatly enhance the zero phonon line for high-efficiency plant-growth LEDs, *J. Mater. Chem. C*, 2021, **9**, 7163–7173.
- 13 S. Q. Fang, T. C. Lang, T. Han, J. Y. Wang, J. Y. Yang, S. X. Cao, L. L. Peng, B. T. Liu, A. N. Yakovlev and V. I. Korepanov, Zero-thermal-quenching of Mn⁴⁺ far-red-emitting in LaAlO₃ perovskite phosphor via energy compensation of electrons' traps, *Chem. Eng. J.*, 2020, **389**, 124297.
- 14 T. Hu, H. Lin, Y. Cheng, Q. M. Huang, J. Xu, Y. Gao, J. M. Wang and Y. S. Wang, A highly-distorted octahedron with a C_{2v} group symmetry inducing an ultra-intense zero phonon line in Mn⁴⁺-activated oxyfluoride Na₂WO₂F₄, *J. Mater. Chem. C*, 2017, **5**, 10524–10532.
- 15 Y. Li, Y.-Y. Li, K. Sharafudeen, G.-P. Dong, S.-F. Zhou, Z.-J. Ma, M.-Y. Peng and J.-R. Qiu, A strategy for developing near infrared long-persistent phosphors: taking MAIO₃:Mn⁴⁺, Ge⁴⁺ (M = La, Gd) as an example, *J. Mater. Chem. C*, 2014, **2**, 2019–2027.
- 16 S. S. Liang, G. G. Li, P. P. Dang, Y. Wei, H. Z. Lian and J. Lin, Cation substitution induced adjustment on lattice structure and photoluminescence properties of Mg₁₄Ge₅O₂₄:Mn⁴⁺: optimized emission for W-LED and thermometry applications, *Adv. Opt. Mater.*, 2019, **7**, 1900093.
- 17 M. H. Fang, W. L. Wu, Y. Jin, T. Lesniewski, S. Mahlik, M. Grinberg, M. G. Brik, A. M. Srivastava, C. Y. Chiang, W. Zhou, D. Jeong, S. H. Kim, G. Leniec, S. M. Kaczmarek, H. S. Sheu and R. S. Liu, Control of luminescence by tuning of crystal symmetry and local structure in Mn⁴⁺-activated narrow band fluoride phosphors, *Angew. Chem., Int. Ed.*, 2018, **57**, 1797–1801.
- 18 M. H. Du, Chemical trends of Mn⁴⁺ emission in solids, *J. Mater. Chem. C*, 2014, **2**, 2475–2481.
- 19 K. Saritas, W. M. Ming, M. H. Du and F. A. Reboredo, Excitation energies of localized correlated defects via quantum Monte Carlo: a case study of Mn⁴⁺-doped phosphors, *J. Phys. Chem. Lett.*, 2019, **10**, 67–74.
- 20 D. Fukuda, Microstructure and photoluminescence properties of Mg-doped BaTiO₃:Pr³⁺ phosphors, *J. Am. Ceram. Soc.*, 2007, **90**, 2670–2672.
- 21 G. Gasparotto, L. Tavares, T. Silva, L. Maia and J. Garvalho, Structural and spectroscopic properties of Eu³⁺ doped Y₄Al₂O₉ compounds through a soft chemical process, *J. Lumin.*, 2018, **204**, 513–519.
- 22 T. Ungár, Microstructural parameters from X-ray diffraction peak broadening, *Scr. Mater.*, 2004, **51**, 777–781.
- 23 M. S. Cai, T. C. Lang, T. Han, D. Valiev, S. Q. Fang, C. Z. Guo, S. S. He, L. L. Peng, S. X. Cao, B. T. Liu, L. Du, Y. Zhong and E. Polissadova, Novel cyan-green-emitting Bi³⁺-doped BaScO₂F, R⁺ (R = Na, K, Rb) perovskite used for achieving full-visible-spectrum LED lighting, *Inorg. Chem.*, 2021, **60**, 15519–15528.
- 24 S. Hariyani and J. Brgoch, Local structure distortion induced broad band emission in the all-inorganic BaScO₂F:Eu²⁺ perovskite, *Chem. Mater.*, 2020, **32**, 6640–6649.
- 25 J. Q. Chen, C. H. Yang, Y. B. Chen, J. He, Z.-Q. Liu, J. Wang and J. L. Zhang, Local structure modulation induced highly efficient far-red luminescence of La_{1-x}Lu_xAlO₃:Mn⁴⁺ for plant cultivation, *Inorg. Chem.*, 2019, **58**, 8379–8387.
- 26 G. X. Li, G. Li, Q. Mao, L. Pei, H. Yu, M. J. Liu, L. Chu and J. S. Zhong, Efficient luminescence lifetime thermometry with enhanced Mn⁴⁺-activated BaLaCa_{1-x}MgxSbO₆ red phosphors, *Chem. Eng. J.*, 2022, **430**, 132923.
- 27 Z.-Q. Ye, S.-G. Xiao and X.-L. Yang, Up-conversion of Nd³⁺/Yb³⁺/Tm³⁺ tri-doped CaTeO₃ compound under excitation of 808 nm, *Rare Met.*, 2021, **40**, 1008–1013.
- 28 L. Ma, Z. G. Xia, V. Atuchin, M. Molokeev, S. Auluck, A. H. Reshak and Q. L. Liu, Engineering oxygen vacancies towards self-activated BaLuAl_xZn_{4-x}O_{7-(1-x)/2} photoluminescent materials: An experimental and theoretical analysis, *Phys. Chem. Chem. Phys.*, 2015, **17**, 31188–31194.
- 29 V. Atuchin, L. Isaenko, V. Kesler, M. Molokeev, A. Yelissev and S. Zhurkov, Exploration on anion ordering, optical properties and electronic structure in K₃WO₃F₃ elpasolite, *J. Solid State Chem.*, 2012, **187**, 159–164.
- 30 H. P. Ji, Z. H. Huang, Z. G. Xia, M. S. Molokeev, X. X. Jiang, Z. S. Lin and V. V. Atuchin, Comparative investigations of the crystal structure and photoluminescence property of eulytite-type Ba₃Eu(PO₄)₃ and Sr₃Eu(PO₄)₃, *Dalton Trans.*, 2015, **44**, 7679–7686.
- 31 S. Y. Li, Q. Zhu, J. Q. Xiahou and J.-G. Li, Doping Pb²⁺ in LaAlO₃ to generate dual emission centers and an optical storage container for visible and near infrared persistent luminescence, *Dalton Trans.*, 2022, **51**, 1112–1122.
- 32 Y. Zhou, X. M. Wang, C. P. Wang, T. Zhang, Y. G. Wang, F. Dou and H. Jiao, A strong zero-phonon line red phosphor BaNbF₇:Mn⁴⁺ for white LEDs, *Inorg. Chem. Front.*, 2020, **7**, 3371–3378.
- 33 T. S. Sreena, P. P. Rao, A. K. V. Raj and T. R. A. Thara, Exploitation of Eu³⁺ red luminescence through order-dis-

- order structural transitions in lanthanide stannate pyrochlores for warm white LED applications, *Phys. Chem. Chem. Phys.*, 2018, **20**, 24287–24299.
- 34 Q. Zhou, J. Wan, Y. Y. Zhou, S. Zhang, D. X. Shi, X. L. Xie, H. Q. Pu, Y. Q. Ye and Z. L. Wang, Ultraintense zero-phonon line from a Mn^{4+} red-emitting phosphor for high-quality backlight display applications, *Inorg. Chem.*, 2021, **60**, 19197–19205.
- 35 J. A. Nelson, E. L. Brant and M. J. Wagner, Nanocrystalline $\text{Y}_2\text{O}_3:\text{Eu}$ phosphors prepared by alkalide reduction, *Chem. Mater.*, 2003, **15**, 688–693.
- 36 H. P. Ji, Z. H. Huang, Z. G. Xia, M. S. Molokeev, M. Y. Chen, V. V. Atuchin, M. H. Fang, Y. G. Liu and X. W. Wu, Phase transformation in $\text{Ca}_3(\text{PO}_4)_2:\text{Eu}^{2+}$ via the controlled quenching and increased Eu^{2+} content: identification of new cyan-emitting $\alpha\text{-Ca}_3(\text{PO}_4)_2:\text{Eu}^{2+}$ phosphor, *J. Am. Ceram. Soc.*, 2015, **98**, 3280–3284.
- 37 Y. Wei, C. C. Lin, Z. W. Quan, M. S. Molokeev, V. V. Atuchin, T.-S. Chan, J. Lin and G. G. Li, Structural evolution induced preferential occupancy of designated cation sites by Eu^{2+} in $\text{M}_5(\text{Si}_3\text{O}_9)_2$ ($\text{M} = \text{Sr}, \text{Ba}, \text{Y}, \text{Mn}$) phosphors, *RSC Adv.*, 2016, **6**, 57261–57265.
- 38 G. G. Li, C. C. Lin, W.-T. Chen, M. S. Molokeev, V. V. Atuchin, C.-Y. Chiang, W. Z. Zhou, C.-W. Wang, W.-H. Li, H.-S. Sheu, T.-S. Chan, C. G. Ma and R. S. Liu, Photoluminescence tuning via cation substitution in oxonitridosilicate phosphors: DFT calculations, different site occupations, and luminescence mechanisms, *Chem. Mater.*, 2014, **26**, 2991–3001.
- 39 S. Q. Fang, T. C. Lang, T. Han, M. S. Cai, S. X. Cao, L. L. Peng, B. T. Liu, Y. Zhong, A. N. Yakovlev and V. I. Korepanov, A novel efficient single-phase dual-emission phosphor with high resemblance to the photosynthetic spectrum of chlorophyll A and B, *J. Mater. Chem. C*, 2020, **8**, 6245–6253.